The optical challenge of two-colour lunar laser ranging at MéO station

Gregoire Martinot-Lagarde, Hervé Mariey, N. Maurice, J. Scariot, H. Viot

Results in Optics 21 (2025) 100833

Contents lists available at ScienceDirect

Results in Optics

journal homepage: www.sciencedirect.com/journal/results-in-optics

The optical challenge of two-colour lunar laser ranging at MéO station

G. Martinot-Lagarde *, H. Mariey, N. Maurice, J. Scariot, H. Viot

Université Côte d'Azur, CNRS, Observatoire de la Côte d'Azur, IRD, Géoazur UMR 7329, 2130 route de l'Observatoire, 06460 Caussols, France

A B S T R A C T

This article describes recent optical developments for the Nd:YAG laser at the MéO station, which regularly carries out **L**unar/**S**atellite Laser Ranging (**LLR**/**SLR**) observations for fundamental physics and space geodesy. MéO (registred as GRSM 7845 in the International Laser Ranging Service network) ranges to the Moon since 1981 with lasers undergoing continuous development for improved reliability. Since 2012, a 150 ps pulsed laser version has provided reliable green LLR. Infrared LLR followed from 2015 and two-colour ranging started recently. This work focuses on the recent optical improvements to this laser to achieve this two-colour capability. There, the Paraxial Gaussian Beam tool of the *Zemax OpticStudio* software models the evolution of the beam shape throughout its propagation inside the station. This enhanced optical set-up drastically improved the lifetime of the biggest rod of the amplification chain, cancelled an annoying thermal pointing drift and supressed infrared vignetting. In 2023, these developments provided 91 two-colour LLR observations for lunar heights greater than 32°. Finally, the text suggests two perspectives for achieving two-colour LLR for Moon heights below 32°.

1. Introduction

The GRSM 7845 laser ranging station, located on the Calern site of the "Observatoire de la Côte d'Azur", is one of 44 active stations in the ILRS (International Laser Ranging Service) network. Each active station mainly collects Satellite Laser Ranging (SLR) data for geodesy. This station (whose alias name is MéO) is also a major player in the field of Lunar Laser Ranging (LLR) (Chabé, 2020). Its current leadership in LLR is based on continuous developments over four decades. Presently, it comprises a Nd:YAG laser, a coudé train, a diffraction-limited telescope (aperture diameter $\varnothing_1 = 1.5$ m) with fine tracking (pointing jitter < 0.1 arcsecond), two avalanche photo-detectors (to collect green and infrared echoes simultaneously under favourable observing conditions), precise event timers and stable clocks (to convert each time-of-flight observation into satellite/lunar orbital parameters).

Here, we present recent improvements to the Nd:YAG laser since the publication of (Martinot-Lagarde, 2016), where a mono-dimensional thermal lensing formalism, derived from (Koechner, 1970), adequately described the propagation of the emission laser through the three amplifiers (A1, A2 and A3) of the laser table.

These improvements allow us to collect lunar echoes simultaneously at 532 nm and at 1064 nm, while maintaining the intensity of the green beam (still emitted at 10 Hz, with pulses of ~ 150 ps FWHM and with ~ 200 mJ per green pulse). This two-colour LLR capacity is very valuable because it combines lower green detector jitter with improved infrared telemetry sensitivity. Moreover, it opens the way for atmospheric model questioning and two-wavelength correction. In practice, as a motorised tilt (<1°) of the LBO doubler allows the green doubling gain to be adjusted in the range [10 %, 66 %], we now begin LLR observations in the infrared by minimising the doubling gain. Here, green pulses (of ~ 30 mJ) materialise the laser for safety reasons. Then, as soon as the infrared return rate exceeds 10 % of the shots (which typically happens for dry skies, an elevation of the Moon greater than ~32° and a stable atmosphere), we maximise the doubling gain, generating green pulses of 200 mJ and infrared pulses of 100 mJ. This provides two-colour echoes in the preferred single photon mode (as in (Samain, et al., 1998).

This success, boosting space geodesy and fundamental physics applications (Murphy, 2013), required significant rod shifts within the amplification chain (increasing its length by ~30 %), leading to a new analysis of the evolution of the laser profile, exposed hereafter. In section 1, we focus on technological aspects regarding pumping efficiencies and beam fluences inside the laser chain. Section 2 presents the optical configuration from the laser cavity to the sky. In section 3, we outline our general strategy for adequately reproducing the actual laser profiles (in both wavelengths) with the GBP tool of *Zemax* (using a Paraxial Gaussian Beam formalism). Section 4 evaluates the evolution of the beam quality factor (M^2) inside the telemeter. Section 5 characterises and solves a delicate thermal drift of the laser pointing direction. In section 6, we demonstrate why our new configuration suppresses infrared vignetting, leading to 91 successful two-colour LLR observations in 2023 exposed in section 7.

* Corresponding author.
E-mail address: Gregoire.Martinot@oca.eu (G. Martinot-Lagarde).

https://doi.org/10.1016/j.rio.2025.100833
Received 5 December 2024; Received in revised form 15 April 2025; Accepted 21 April 2025
Available online 25 April 2025

1.1. Pumping efficiencies and beam fluences estimations

The laser cavity of the telemeter is pumped by a pair of *Quantel SFL 511–07 RX0.5* flashlamps connected in series, located upon and under a Nd:YAG rod (named A0). Lasing requires powerful flashes of light to excite the rod material, from an electrical discharge of energy, previously stored in a capacitor bank. This bank must first be charged to a maximum voltage (U_{A0}), slightly exceeding the Lasing Threshold voltage (LT). When new lamps pump A0, LT is minimal (and named LT_{min}). After several months of operation, LT reaches its maximum permitted value of LT_{max}, with $LT_{max} = 2000$ V.

From February 2012 to January 2022, each lamp provided $\sim$ 15 million shots with $LT_{min} \sim 1550$ V. Then, during 2022, LT_{min} grew steadily towards LT_{max}. This interrupted our LLR observations during several weeks (from 15 February to 23 March 2023). After much trial and error, we suddenly solved the problem by replacing the historical fluid (which stabilised the temperature of the four A# rods below 30 °C) with deionised water. As this cooling water also surrounds the pumping flashlamps, we concluded that the historical fluid propagated a parasitic current leak through degraded connectors (degrading A0 pumping efficiency). Fig. 1 shows this amplifier module, with old cracked flashlamp connectors, recently replaced by new ones to enforce their electric isolation.

The insertion of this repaired amplifying module inside the cavity procured immediately a record minimal lasing threshold of 1500 V (instead of 1550 V). So, we awaited that this 50 V widening of the available voltage domain would increase the flashlamp lifetime of 11 % ($\approx$ 50/450). Surprisingly, the lamp life doubled (providing exceptionally 30 million of shots instead of 15 millions). It reveals that the lifespan of those lamps highly depends on their physical environment.

Simultaneously, this refurbishment of the A0 pump module resulted in weaker optical pulses at the cavity output (0.5 mJ instead of 1 mJ). This significant loss in energy of this cavity pulse is unexplained as this global cavity makeover modified five components: the cooling water, the pumping module, electronic elements of its power supply, a fan of the primary cooling circuit and the cavity alignment.

Anyway, we consider those weaker cavity pulses to be an advantage, as it reduces the beam fluence inside the cavity, limiting laser damage risks on optical surfaces inside this cavity. Moreover, low energy pulses usually exhibit very good beam qualities factors (as illustrated in section 4). Finally, this 2023 version of the cavity should reach its emission threshold with reduced pumping energy.

Table 1 exposes the evolution of Beam Fluences (BF) upon the optical table. Those BF values are established with a simplified hat beam formalism, where a uniform beam of radius $\rho_{uniform}$ carries the energy of the infrared pulse with $\rho_{uniform} = w_0$ inside the cavity and with $\rho_{uniform} = 0.5\ \varnothing_{A\#} - 0.5$ mm in the three rods of the amplification chain of diameter $\varnothing_{A\#}$ ($\varnothing_{A1} = 7$ mm, $\varnothing_{A2} = 9.52$ mm, $\varnothing_{A3} = 12.7$ mm). As the beam travels back and forth inside the cavity, the internal elements of that cavity experience two fluences: a forward fluence (towards the sky) and a backward fluence (towards the rear mirror of the cavity). Since the risk of optical damage depends on the maximum fluences, we enter these maximum fluences in the last column of Table 1 (where BF = pulse_energy_written_in_bold_letters/[$\pi\ \rho^2_{uniform}$]).

To determine these fluences, we first estimated the transmission of each optical element in the cavity, called T_X for each element X where $T_X \leq 1$. For each amplifier module A#, we use the notation $G_{A\#}$ (instead of $T_{A\#}$) to illustrate that the gain of each amplifier ($G_{A\#}$) is systematically greater than 1.

Table 1 shows that the laser still delivers 300 mJ at the output of the amplification chain, thanks to the increase in the common voltage of {A1 + A2} from $U_1 = 1.6$ kV to $U_2 = 1.9$ kV. This doubling of energy, obtained solely from this moderate 19 % voltage increase (feeding A1 and A2) surprised us at first, because it reveals that the relationship between $U_{A\#}$ and $G_{A\#}$ is not linear. More precisely, we have:

$$\frac{G_{A1}(U_2)}{G_{A1}(U_1)} = \frac{30}{20} = 1.5 \ \geq \ \left(\frac{U_2}{U_1}\right)^2 = 1.41 \ \geq \ \frac{G_{A2}(U_2)}{G_{A2}(U_1)} = \frac{10}{7.5}$$
$$= 1.33 \ \Rightarrow \ \frac{G_{A1}(U_2)}{G_{A1}(U_1)} \times \frac{G_{A2}(U_2)}{G_{A2}(U_1)} \ \sim \ 2 \qquad (1)$$

Eq. (1) shows that A1 contributes 6 % more than A2 to this overall doubling of the gain by {A1 + A2}. Since $BF_{A2} \approx 5\ BF_{A1}$ (according to Table 1), we believe that a progressive saturation of optical gain in this chain generates this slight decrease in gain from A1 to A2.

As Table 1 also procures $BF_{A0} \sim BF_{A1}$ and $BF_{A3} \sim BF_{A2}$, it becomes relevant to deduce that all A# rods have their gains ($G_{A\#}$) quasi-proportional to $U^2_{A\#}$. This property is consistent with estimating that each pair of lamps mainly receives the energy of the complete discharge ($\sim 0.5C\ U^2_{A\#}$) from its bank of capacitors with C = 30μF (located in each *QUANTEL CB631* or and in each *BMI SE.051* rack).

In section 4, as thermal lensing depends directly on the $P_{A\#}$ pump power supplied to each rod, we need to add the contribution of the simmer circuit (reducing the inductance of those lamps) which contributes to the rod heating with P_{simmer}. (Yee, 1979) proposed a pre-pulsing technique to obtain $P_{simmer} \ll P_{A\#}$. As our laser operates with a quasi-continuous simmer, P_{simmer} might be slightly higher. However, it remains significantly lower than $P_{A\#}$ because its presence heats the cooling water of less than 0.2 °C (where the laser firing increases the cooling water temperature of several degrees). Since P_{simmer} is factory-set, it remains constant. We estimate that $P_{simmer} \approx 41$ W, as this value generates a perfect TEM_{00} beam at the minimum lasing threshold of 1500 V (see Table 3). Therefore, as soon as the laser fires (with Rate = 10 Hz), the overall pump power supplying each pair of flashlamps surrounding any rod A# is:

Fig. 1. Front and side vues of MéO A0 amplifier (with cracked flashlamp connectors).

Table 1
Typical Beam Fluences of the infrared pulse upon the laser table (in a hat beam formalism).

Optical element	**T**ransmission (T) or **G**ain (G)	Forward output pulse energy in mJ	Backward input pulse energy in mJ	Approximate beam radius $\rho_{uniform}$ in mm	**B**eam **F**luence (BF) in J/cm^2
Rear mirror	0	0.391	**0.391**	0.7	0.0254
TFPN polariser	~ 0.95	0.372	**0.412**	0.7	0.0268
Cr^{4+}:YAG crystal	0.83*	0.308	**0.496**	0.7	0.0322
A0	≈ 2.71**	**0.835**	0.183	0.7	0.0542
Diaphragm (STOP)	0.9 (as in (Martinot-Lagarde, 2016)	**0.752**	0.203	0.7	0.0489
Acousto-Optic Modulator (AOM)	~ 0.95	**0.714**	0.214	0.7	0.0464
Fabry-Perot (FP)	0.7***	**0.5**	0	0.7	0.0325
A1	30	**15**	0	3	0.0531
A2	10	**150**	0	4.26	0.263
A3	2	**300**	0	5.85	0.279

* *In 2015, this transmission was established with an additional Cr4$^+$:YAG crystal located out of the cavity and submitted to a fluence of* ~ 0.0325 J/cm^2 *procuring*: $T_{Cr^{4+}}$ = 248 mJ / 300 mJ = 0.827 ~ 0.83.

** $(T_{TFPN} \times T_{Cr^{4+}} \times G_{A0} \times T_{STOP} \times T_{AOM})^2 \times (1 - T_{FP}) = 1$ *after a beam round-trip* ⇒ $G_{A0} \approx 2.71$.

*** $T_{FP} = 0.7$ *is also the Fabry-Perot transmission of the Nd:Yag output mirrors in* Lucchini (1995) *and in* (Yee, 1979).

$$P_{A\#} = \text{Rate} \times \frac{1}{2} C U_{A\#}^2 + P_{simmer} = 150\,W \times \left(\frac{U_{A\#}}{1kV}\right)^2 + 41W \qquad (2)$$

Eq. (2) only holds with fresh flashlamps implemented. Indeed, when $U_{A\#}$ rises steadily to compensate for lamp ageing, $P_{A\#}$ and related parameters such as $G_{A\#}$ and thermal lensing effects remain constant.

1.2. Description of the optical configuration of MéO two-colour laser

Fig. 2 shows the optical propagation of the laser from the rear cavity mirror to the sky, with using the alphabetic order along the propagation as much as possible. However, as this telemeter comprises a big amount of optical elements, several mirrors were also named with the notation M_n with n∈{1; 8}, where the telescope secondary mirror M_2 {$\varnothing_{2optical}$ /$\varnothing_{2mec.}$ = 290 mm/320 mm, 44 mm thick} is element W and where the primary mirror M_1 {$\varnothing_{1optical}$ /$\varnothing_{1mec.}$ = 1500 mm/1544 mm, 180 mm thick} is element Z.

Fig. 2(a) is a top view of the laser table from the rear mirror (A) to the bottom mirror of the periscope (T). There, this mirror (T) is dummy, to superimpose a side view of the periscope (T + M_8) on Fig. 2(a). Then, Fig. 2(b) is a perspective view of the rest of the telemeter from M_8 (drawn in red) to the sky.

On Fig. 2(a), we have enlarged all refractive optical elements to highlight for example the reversed orientation of lens J, suppressing (as in (Martinot-Lagarde, 2016) a ghost image inside rod A2 (=element M). Moreover, the amplifying chain of this laser has only two beam expanders (instead of three used in (Martinot-Lagarde, 2016). This elimination of the intermediate beam expander considerably extends the life of the last rod (A3 = N), since optical damage to its output face centre only appeared after two years (instead of two months).

Table 2 characterises precisely the complete laser travel from the laser room to the sky. The first column contains the longitudinal position (z_X) of each optical element X relative to the Fabry-Perot filter centre (G). Each refractive element X has its centre at z_X. For reflective elements, z_X specifies the centre of their optical surface. As this axis is oriented towards the sky, we get $z_X < 0$ in the cavity and $z_X > 0$ outside of it. This z-axis offers a convenient way to estimate the size of each part of MéO station:

- The infrared beam travel upon the laser table is: $z_T - z_A$ = 9500 mm + 938 mm ≈ 10.44 m,
- Then, its travel from the laser room to the telescope is: $z_v - z_T \approx$ 11.5 m, where V is a motorised diverging lens (also drawn in red in Fig. 2 (b)) that pilots the sky divergence of the laser.
- Finally, the remaining travel of the beam is $z_{sky} - z_V$ = (33540.4 − 21003.5)mm ≈ 12.54 m.

Consequently, the complete path of the laser (of ~ 34.5 m) comprises three portions of similar lengths: one on the laser table, a second through the focal laboratory and a third one inside the telescope structure.

The last column of Table 2 contains $1/e^2$ laser radiuses from the *Zemax* Gaussian Beam Paraxial Size (GBPS) operand, with infrared values ($w(z_X)$) on its left and green values ($s(z_X)$) on its right.

In Table 2, the beam fills quasi-entirely the surface of each rod of the amplification chain (with security margins similar to the 0.5 mm margin used in Table 1), as Table 2 simulation gives: A1_margin = 0.5 $\varnothing_{A1}$ − w(z_K) = 0.45 mm, A2_margin = 0.5 $\varnothing_{A2}$ − w(z_M) = 0.43 mm and A3_margin = 0.5 $\varnothing_{A3}$ − w(z_N) = 0.34 mm. Moreover, the quasi-equality of sizes of both beams after the LBO crystal (P) illustrates already that this configuration no longer vignettes the infrared beam (see section 6). In the two next sections, we outline our strategy for fitting the profile values in Table 2 to the real laser.

1.3. General strategy to emulate MéO two-colour laser propagation

The laser table (represented on Fig. 2), is a *Newport RP Reliance* honeycomb optical table (0.2 m thick and 2.4 × 1.4 m^2 in area) located in a dedicated air-conditioned room, under a laminar flow hood (reducing dust pollution). We then consider that its horizontal surface defines a stable plane of incidence for the laser, located approximately 60 mm above its stainless steel surface.

Our global reference frame is {O,x,y,z} = {G,x,y,z} in the notation of Fig. 2. Since proper laser alignment corresponds to the laser passing through the centre of each optical element (defining the z-axis), the centre of the laser beam nominally coincides with this optical z-axis from the cavity to the sky. Moreover, even though the notation of Fig. 2 has the advantage of respecting the alphabet order along the telemeter, we will use henceforth the four amplifiers names {A0, A1, A2, A3}, instead of the reference letters {D,K,M,N} in Fig. 2, to comply with section 1 of this document.

Inside the cavity, the x-axis is horizontal and the y-axis is the vertical altitude above the plane of incidence. Outside the cavity, when the beam profile turns out to be locally slightly elliptical, we define the x-axis along the minor axis of the beam footprint (and the y-axis along its major axis). The beam polarisation is initially horizontal inside the cavity. Then, the half-wave plate (L), located between rods A1 and A2, turns it vertical to cancel the polarisation impact on thermal lensing by rods (as in (Martinot-Lagarde, 2016). Moreover, the circular shape of the diaphragm and of all the rods also favours the circularisation of the laser. This consolidates the relevance of our axially symmetric modelling developed here with the intensive use of the radial coordinate ρ (where $\rho = \sqrt{x^2 + y^2}$), to emulate the propagation of the laser.

In following equations, the wavelength λ is replaced by either λ_1 =

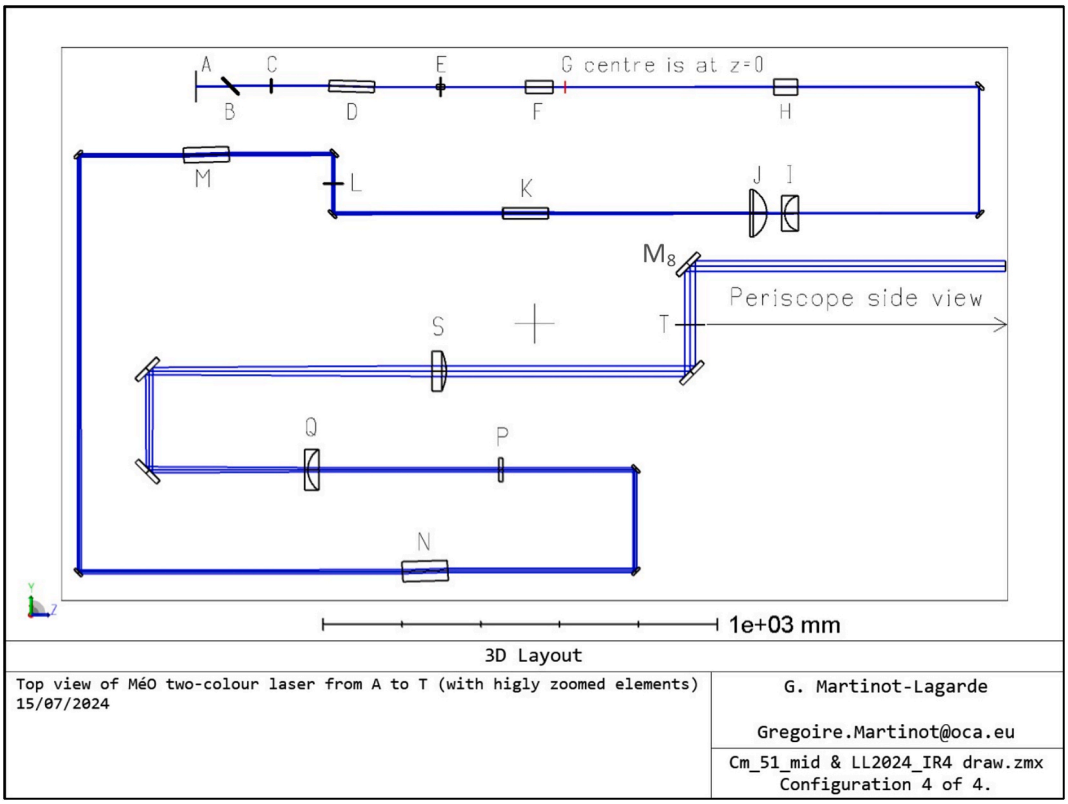

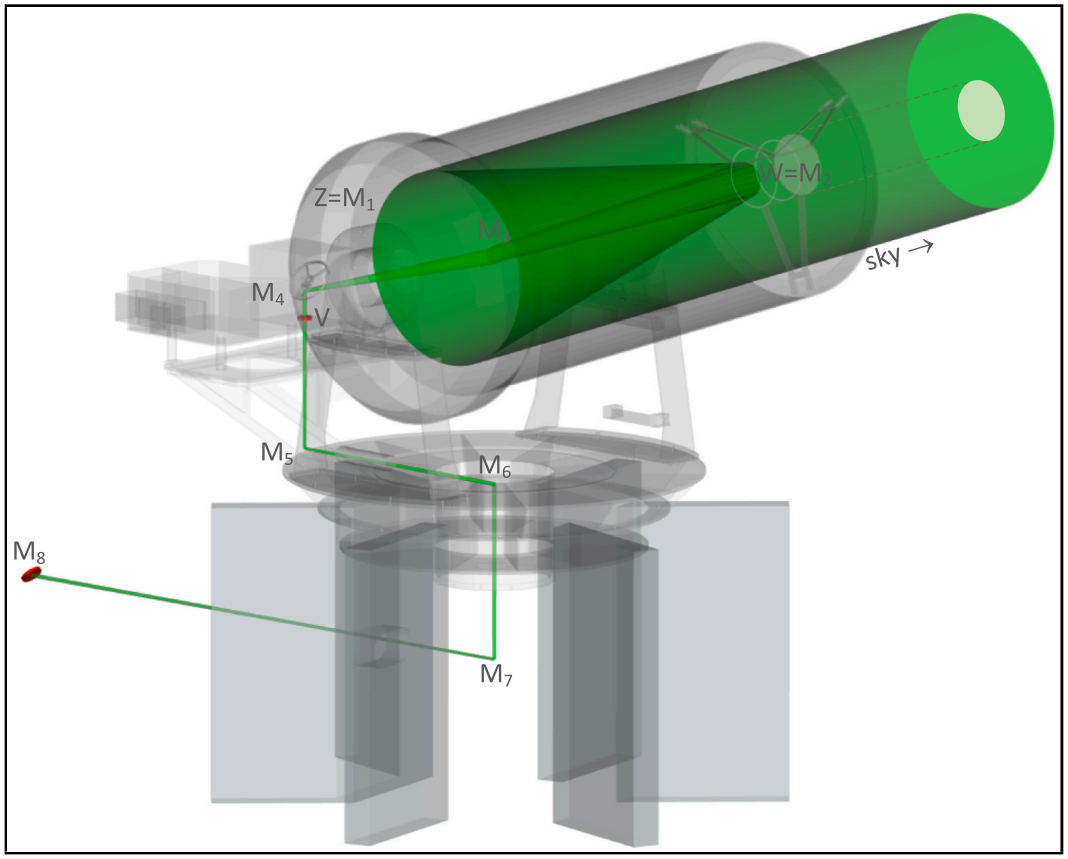

Fig. 2. Fig. 2**(a).** Top view of MéO laser table, with reference letters "X" specified in Table 2. Fig. 2**(b).** 3D view of the propagation of the green beam from the top of the periscope (M_8) to the sky.

Table 2
Zemax design of MéO. Here, column 6 uses a square brackets convention where]XY[is the usual air distance between element X and Y. However, if Y is a refractive optic (such as element B),]XY] specifies the distance from the vertex of the exit surface of element X to the centre of element Y.

Element X & coordinate z_X in mm	Function of element X {with aperture, tilt or additional information}	*Zemax* material	Element X thickness in mm	1rst | 2nd radius of curvature in mm	Distance to next element (along z) in mm	$1/e^2$ laser radiuses $w(z_X)$ | $s(z_X)$ in mm
A − 938	Rear mirror of the cavity	mirror	6.35	∞	]AB] = 88.5	
B − 849.5	TFPN *cvilaseroptics* polariser	SILICA	6.35	∞	[BC[= 101.5	
C − 746	Cr^{4+}:YAG crystal {4.5 × 4.5 mm^2}	IRG3	4	∞	]CD[= 145	
D − 541.5	Rod A0 {$\varnothing_{A0}$ = 7 mm & 3.638°}	IRG3	115	±8515	]DE] = 168	
E − 316	Diaphragm {$\varnothing_{STOP}$ = 1.5 mm}	Teflon	0		[EF[= 216	
F − 65.75	*IntraAction* AOM	SILICA	68.5	∞	]FG] = 31.5	
G 0	Fabry-Perot filter	SILICA	0.35	∞	[GH[= 530	0.7 | 0.495
H 560	Pulse picker	SILICA	60	∞	]HI[=1273	0.76 | 0.54
I 1864	Diverging lens {with *Zemax*,]IJ[(λ_1) ≠]I,J[(λ_2) ⇐ $s(z_P) \approx w(z_P)$}	S-BSL7	2	−46.71|∞	]I,J[(λ_1) = 37.5]I,J[(λ_2) = 28.5	1.23 | 0.87
J 1898.35	Converging lens {]IJ[real ~ 33 mm}	SILICA	2.7	69 | ∞	]IK[= 588	1.75 | 1.16
K 2510.5	Rod A1 ⇔ A0 (upward tilted)	IRG3	115	±5868	]KL[= 503.5	3.05 | 2.41
L 3073	Half wave plate at λ_1	SILICA	3	∞	]LM[= 338.5	3.82 | 3.21
M 3470.5	Rod A2{$\varnothing_{A2}$ = 9.52 mm & 3.638°}	IRG3	115	±10853	]MN[= 2140	4.33 | 3.74
N 5725.5	Rod A3{$\varnothing_{A3}$ = 12.7 mm & 3.638°}	IRG3	115	±36116	]NP[= 1065	6.01 | 5.68
P 6853	LBO doubler	LF8	10	∞	]PQ[= 485	6.55 | 6.35
Q 7347	Diverging lens	F_SILICA	8	−627.5|∞	]QS[≈ 1361.5	6.80 | 6.67
S 8731	Converging lens	F_SILICA	6	∞|−1190.18	]ST[= 766	14.13 | 14.19
T 9500	Periscope bottom and top mirrors{$\varnothing_{mec.}$ =	UVFS	12.7	∞	]T M_8[= 149	14.15 | 14.20
M_8 9649	76.2 mm & 45°}	UVFS	12.7	∞	]M_8 M_7[= 6550	14.15 | 14.20
M_7 16,199	Mirror {$\varnothing_{mec.}$ = 201 mm & 45°}	Zerodur	34	∞	]M_7 M_6[= 1934	14.22 | 14.20
M_6 18,133	Mirror{$\varnothing_{mec.}$ = 201 mm & 52.5°}	Zerodur	34	∞	]M_6 M_5[= 1632	14.24 | 14.19
M_5 19,765	Mirror{$\varnothing_{mec.}$ = 76.2 mm & 52.5°}	UVFS	12.7	∞	]M_5 V[= 1236	14.26 | 14.19
choice of]TV[best	**The best two-colour LLR configuration is when]TV[=]TV[best = 11501 mm**]TV[Green collimation = 11497 mm ≠]TV[Infrared collimation = 11513 mm ⇒ Green plain-angle div. ~ 5.3as					
V 21003.5	Diverging lens {$\varnothing_{mec.}$ = 50.8 mm }	F_SILICA	5.036	−303.8|∞	]M_5 M_4[= 1374	14.31 | 14.23
M_4 21,139	Mirror {$\varnothing_{mec.}$ = 60 mm & 45°}	UVFS	12.7	∞	]M_4 M_3[= 1873	17.16 | 17.13
M_3 23,012	$\varnothing_{opt.}$ /$\varnothing_{mec.}$ = 330 mm/360 mm & 45°	Zerodur	65	∞	]M_3 W[= 3055	56.75 | 57.43
W 26,067	The *Zemax* paraxial surface with f_W = − 977.959 mm models M_2				]W Z[≈ 3736.7	121.3 | 123.2
Z 29803.7	The *Zemax* paraxial surface with f_Z = 4572 mm models M_1				]Z sky[≈3736.7	675.7 | 685.7
sky 33540.4	⇒ The total track from A to the sky is $z_{sky} - z_A$ = 33540.4 mm + 938 mm ≈ 34478 mm ~ 34.5 *m*					

1064 nm or by $\lambda_2 = 532$ nm when each wavelength is to be specified, to study specifically the infrared (w(z)) or the green (s(z)) profile.

In addition, even though the green beam emanates from the LBO doubling crystal, whose centre is located quite far from the cavity (at $z_P \approx 6853$ mm), we simulate both beams diverging from z = 0, which facilitates *Zemax* files parameterisations and allows additional beam shape comparisons.

The infrared beamwaist (w_0) is identical to the waist determined in (Martinot-Lagarde, 2016) as our cavity rejuvenation preserved its nominal geometry. For the green beam, we define a virtual beamwaist s_0 from w_0 with:

$$w_0 = w(0) = 0.7\ \text{mm} \ \text{ and } \ s_0 = w_0\sqrt{\lambda_2/\lambda_1} = w_0/\sqrt{2} \Rightarrow s_0 = s(0) = 0.495\ \text{mm} \quad (3)$$

This strategy succeeds in superimposing the emulated beam sizes (from Table 2) on the real beam sizes, with reasonable adjustments to the experimental values of]IJ[,]QS[, and]TV[.

Finally, we systematically favour circularised beam quality factors $M^2(z)$ rather than elliptical ones, even if $M_x^2(z) \neq M_y^2(z)$, with the (surface-conserving) equation: $M^2(z) = M_x(z)\, M_y(z)$.

1.4. Modelling of the evolution of the beam quality factor inside the telemeter

In theory, a pure Gaussian laser of wavelength λ, propagating itself in free space (from z = 0 and along the z-axis) diverges from its waist radius $w_{Gaussian}$ with a beam fluence decreasing from I_0 with:

$$I_{Gaussian}(\rho, z) = I_0\, e^{-2\left(\frac{\rho}{w_{Gaussian}(z)}\right)^2} \ \text{with}\ w_{Gaussian}(z)^2 = w_{Gaussian}^2\left[1 + \left(\frac{\lambda z}{\pi w_{Gaussian}^2}\right)^2\right] \quad (4)$$

As soon as the laser beam deviates from this ideal case, we approximate it by a profile remaining Gaussian, but occupying a wider radial space w(z), characterised by a quality factor $M^2 > 1$, where:

$$I(\rho, z) = I_0 e^{-2\left(\frac{\rho}{w(z)}\right)^2} \ \text{with}\ w(z)^2 = w_0^2\left[1 + \left(\frac{\lambda M^2 z}{\pi w_0^2}\right)^2\right] = w_0^2\left[1 + \left(\frac{z}{z_R}\right)^2\right] \quad (5)$$

Eq. (5) illustrates that the propagation of such quasi-Gaussian beam remains determined by two parameters: its beamwaist (w_0) and its Rayleigh range ($z_R = \pi\, w_0^2\, \lambda^{-1}\, M^{-2}$, with π = Archimedes constant).

In practice, for *Zemax* calculation of quasi-Gaussian laser profiles (where $M^2 > 1$), the GBPS tool delivers also the sizes of a specific pure Gaussian beam, propagating along the same z-axis and possessing the same Rayleigh range. Eq. (6) shows that this Rayleigh range invariance generates that both beams (whose common beamwaist location is at z = 0) possess also the same on-axis wavefront radius of curvature R(z) after any free space propagation along the z-axis (with $z \neq 0$):

$$z_R = \frac{\pi w_0^2}{\lambda M^2} \ \text{invariance} \ \Leftrightarrow \ R(z) = z\left[1 + \left(\frac{z_R}{z}\right)^2\right] \ \text{invariance for any fixed}\ z \neq 0 \quad (6)$$

If the beam quality factors remain identical at both wavelengths (which we assume below), our choice of s_0 (made in Eq. (3)) also results in such Rayleigh range invariance, leading to $R_{green} = R_{infrared}$ near G.

Independently, Eq. (6) enables us to estimate M^2 inside the cavity. Indeed, if we simulate the round trip propagation of a pure Gaussian beam inside the cavity from z = 0 (with one reflection on the cavity rear mirror and return to z = 0), we obtain a unique beamwaist value ($w_{Gaussian}$), whose return footprint size matches exactly the initial one. How realistic is that pure Gaussian laser?

For those *Zemax* simulations, we removed the 1.5 mm diameter diaphragm (normally present in the cavity), to respect the fact that the local fluence of any pure Gaussian beam is always strictly positive (as in Eq. (4)). Therefore, as this internal diaphragm is vital to stabilise the telemeter pointing direction in the sky, we know that this pure Gaussian beam is not accessible in practice.

However, if we consider that the practical inclusion of this diaphragm in the cavity perturbs significantly more beam sizes than beam wavefronts (being severely constrained by cavity geometry), we can then apply Eq. (6) equivalence, leading to:

$$z_R = \frac{\pi w_0^2}{\lambda M^2_{Cavity}} \approx z_{R\,Gaussian} = \frac{\pi w^2_{Gaussian}}{\lambda} \Rightarrow M^2_{Cavity} \approx \left(\frac{w_0}{w_{Gaussian}}\right)^2 \quad (7)$$

There is one last delicate point to consider. The cavity is equipped with a saturable absorber (Cr^{4+}:YAG) providing effective mode locking with 5 output pulses of 150 ps FWHM. Its passive mode locking initially stabilises the 150 ps duration of this quasi-Gaussian laser pulse, with optical transmission potentially increasing from less than 30 % to ~ 98 % with the increase in light fluence. However, as the spatial profile of this cavity beam is quasi-Gaussian (Martinot-Lagarde, 2016), a similar radial compression of this beam must coexist in the crystal (the weakest off-axis rays being the most attenuated).

As this Cr^{4+}:YAG crystal acts twice on each pulse round trip (inside the cavity), we need to consider the two-way crystal transmission $T^2_{Cr^{4+}}$ (instead of $T_{Cr^{4+}}$). A straightforward way for realising this two-way attenuation by the crystal (while preserving the two-dimensional, quasi-Gaussian profile of the beam) is to postulate that the real beam retains its on-axis fluence, but only undergoes a radial narrowing of its luminous fluence by a factor equal to the one-way transmittance of the crystal ($T_{Cr^{4+}}$).

Finally, as our determinations of $w_{Gaussian}$ (by *Zemax* simulations) are performed without this global Cr^{4+}:YAG shrinkage effect, we need to replace our real beamwaist (w_0) with a fictitious expanded beamwaist (w_0') inside Eq. , to estimate M^2_{Cavity} from two unlocked laser cases. This results in:

$$w_0' = w_0/T_{Cr^{4+}} \Rightarrow M^2_{Cavity} \approx \left(\frac{w_0'}{w_{Gaussian}}\right)^2 = \left(\frac{w_0}{w_{Gaussian} \times T_{Cr^{4+}}}\right)^2 \quad \text{with} \quad T_{Cr^{4+}} = 0.827 \quad (8)$$

The first column of Table 3 synthetises our intra-cavity quality factor formalism, where AFL_{A0} is the Averaged thermal Focal Length generated by the A0 rod (calculated as in (Martinot-Lagarde, 2016). Column 2 represents the case where the flashlamp voltage is set to $U_{A0} = LT_{min} =$ 1500 V. In this case, the beam quality is perfect, but the lasing remains highly unstable. If the operator increases U_{A0} to 1600 V, a 10 Hz lasing is guaranteed, but the beam quality deteriorates to $M^2_{Cavity} \sim 1.06$ (as in column 4). The compromise case in column 3 (where $U_{A0} - LT \sim 50$ V) should be experimentally preferred, as it simultaneously ensures a stable 10 Hz lasing with $M^2_{Cavity} \sim 1.03$ (after a short cavity warm-up < 1 min).

Outside the cavity, the beam undergoes further alterations through optical elements (and after passing through atmospheric disturbances), which increases the value of M^2. We quantify this growth by defining $M^2(z)$ as a staircase function with 4 steps:

- The first step is the intra-cavity space where M^2 is minimum because multiple passes through the intra-cavity diaphragm purify the beam wavefront. There, $M^2 = 1.03$ (according to Table 3).
- The second step is from the Fabry-Perot filter to the telescope magnification, where the circularisation of Laser Beam Profiler *LBP HR [5038]* measurements of $w_x(z_{exp}) = 2.024$ mm and $w_y(z_{exp}) = 2.201$ mm made in (Martinot-Lagarde, 2016) (after $z_{exp} = 3690$ mm propagation in free space) gives:

$$M^2_x(z_{exp}) = \frac{\pi w_0^2}{\lambda z_{exp}} \sqrt{\left(\frac{w_x(z_{exp})}{w_0}\right)^2 - 1} = 1.064 \text{ and } M^2_y(z_{exp}) = \frac{\pi w_0^2}{\lambda z_{exp}} \sqrt{\left(\frac{w_y(z_{exp})}{w_0}\right)^2 - 1} = 1.169$$

$$\Rightarrow \quad M^2(\text{from } z = 0 \text{ to } z_W) = M_x(z_{exp}) \times M_y(z_{exp}) = \sqrt{1.064 \times 1.169} \sim 1.115 \quad (9)$$

- The third step begins when the laser reaches a metric size. This occurs at it propagates from the secondary mirror to the primary mirror of the telescope. There, we opt for $M^2 = 1.14$, giving $s(z_z) = 685.7$ mm in Table 2, compatible with the experimental value of 684 mm.
- The final step involves the propagation of the laser from MéO to the Moon, where telescope pointing jitter, central obstruction by the secondary mirror and atmospheric turbulence affect its effective far-field divergence. There, we use $M^2 = 1.17$ as in (Martinot-Lagarde, 2016), bearing in mind that theoretical and experimental work could refine this estimate of the laser quality factor in the future.

The following Table 4 summarises our actual modelling of M^2 along the propagation of the laser.

1.5. Thermal pointing drift

The laser cavity comprises only flat interfaces (as its rear mirror is

Table 3
Evolution of the beam quality factor in the cavity with the voltage gap = U_{A0} – LT.

U_{A0} – LT (with LT = LT_{min} = 1500 V)	0	50 V	100 V
$(r_{A0}/r_0)^2$ with r_0 = 3.1 mm (see (Koechner, 1970))	$(3.5/3.1)^2$	$(3.5/3.1)^2$	$(3.5/3.1)^2$
$P_{A0} = 150\text{ W} \times (U_{A0}/1\text{ kV})^2 + 41$ W	378.5 W	401.375 W	425 W
$AFL_{A0} = (r_{A0}/r_0)^2 \times 1.65\text{ m} \times 1\text{ kW}/P_{A0}$ (see (Martinot-Lagarde, 2016)	5557 mm	5240 mm	4949 mm
R_{A0} = A0 curvature radius ~ 1.625 × AFL_{A0} ♣	9030 mm	8515 mm	8042 mm
$w_{Gaussian}$	0.846371 mm	0.833235 mm	0.820597 mm
$w_0' = w_0 / T_{Cr4+}$ = 0.7 mm / 0.827	0.846433 mm	0.846433 mm	0.846433 mm
$M^2_{Cavity} = (w_0' / w_{Gaussian})^2$	1.0001 ~ 1	1.032 ~ 1.03	1.064 ~ 1.06

♣ *The factor* 1.625 *converts the* AFL_{A0} *values to the radii of curvature implemented in* Zemax (*instead of the 1.54 factor used in* (Martinot-Lagarde, 2016), *as the* IRG3 *material* (index = 1.817940 in the infrared) *replaces the* N-SF6 (index = 1.773295 used in (Martinot-Lagarde, 2016) *to better match the refractive index of the rods.*

Table 4
Estimations of M^2 for MéO pulsed laser from the rear mirror of the cavity to the Moon.

MéO laser sub-parts	In the laser cavity	Propagation to M_2	Around M_1	After M_1
Achromatic M^2 values	1.03 ± 0.03	1.115	1.14	1.17

also flat). Its optical stability relies on thermal lensing inside the A0 rod (heated by two flashlamps and cooled by lukewarm water flowing along its shell). So, when an observation session begins, the operator has to wait around one minute (of initial warm-up) before a regular 10 Hz lasing settles. Then, for observations lasting more than 10 min, a worrying upward thermal pointing drift (d) occurred on the laser table, exceeding our acceptable angular tolerance (δ_d). After several fruitless investigations, we discovered that it was due to inadequate centring of the cavity stop, as translating this diaphragm upwards by 0.25 mm eliminated it.

Retrospectively, the responsibility of the diaphragm centring (on this drift) is consistent with our finding that tiny misalignments of the cavity very severely affect the beam footprint at the exit of the laser table. We therefore propose to quantify this pointing drift tolerance (δ_d) by assuming that the A0 thermal lensing is solely responsible for this annoying pointing drift. This is equivalent to considering that the overall thermal lensing {A1 + A2 + A3} compensates any diverging impact of {I + J} on laser pointing.

The LBO crystal (15 × 15 mm^2), being the element named P in Fig. 2 (a), has the smallest angular aperture seen from the cavity exit. We therefore define δ_d as the pointing angle that generates acceptable drift of the beam after free-space propagation of $z_P \approx 6853$ mm. According to Table 2, the margin around the local infrared beam at z_P is Margin = 0.5 × $\varnothing_{LBO}$ − $w(z_P)$ = (7.5 − 6.55)mm ≈ 0.95 mm ∼ 1 mm. If the tenth of this Margin defines an acceptable pointing drift, we get:

$$\delta_d = \tan^{-1}(0.1 \times \text{Margin}/z_P) \approx \tan^{-1}(0.1/6853) \approx 3\text{as} \quad (10)$$

This acceptable pointing drift is consistent with our thermal lensing formalism, where a nominal pumping of $U_{A0} = 1550$ V generates an Averaged thermal Focal Length $AFL_{A0} = 5240$ mm (see Table 3). Then, for an aperture offset of $\rho_{stop} \sim 0.25$ mm (relative to A0), this average thermal lensing deflects this off-centre infrared beam by an excessive angular drift d, where:

$$d \approx \tan^{-1}(\rho_{stop}/AFL_{A0}) = \tan^{-1}(0.25/5240) \approx 10\text{as} > \delta_d \quad (11)$$

As we want $|d| < \delta_d$, we need to centre the diaphragm with $\delta\rho_{stop} < \rho_{stop} \times \delta_d / d = 0.25$ mm × 3/10 = 75 μm.

In the search for an appropriate centring of the stop, we investigated the behaviour of the laser when the cavity diaphragm moves vertically in steps of 0.3 mm. By convention: $x_{stop} = y_{stop} = 0$ is our best choice of centring the diaphragm (where the beam footprint leaving the cavity is remarkably symmetrical). In other words, we expect the cavity beam to pass through the centre of the rod in this experimental case. Table 5 and Fig. 3 show the evolution of the Lasing Threshold (LT) with y_{stop}.

The LT curve shows a local maximum of LT near the centre of the rod. It signifies that the pumping efficiency is minimum there. This shows that the temperature of the rod is indeed locally maximum (as the efficiency of an optical amplifier decreases if it is hot). Furthermore, we expected LT(y_{stop}) to be an even function, since the two flashlamps are symmetrically located above and below the rod.

Instead, LT(y_{stop}) exhibits a spurious positive slope, which complicates this experimental test of stop centring. This reveals a slight cooling asymmetry (the flow of water seems to cool the lower part of the rod better). We chose to cancel this parasitic positive slope of LT(y_{stop}) by substracting a linear function (called "Cooling bias") from our raw experimental LT data (with a slope of 12 V/0.3 mm). The "LT − bias" curve (established from the fourth line of Table 5) becomes quasi-

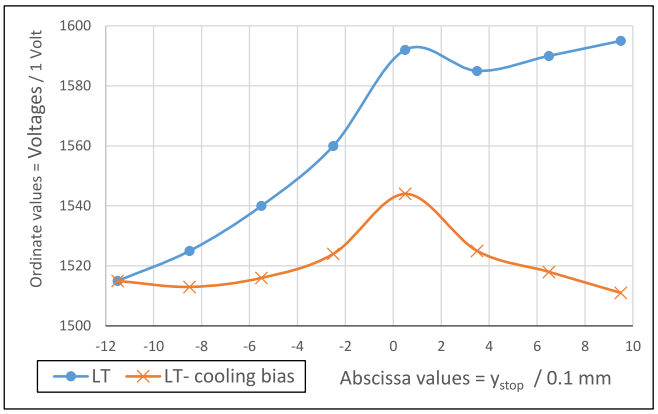

Fig. 3. Lasing Threshold in function of y_{stop} [with (•) and without (×) cooling bias].

symmetric about a vertical axis located at $y_{stop} \approx 0.05$ mm > 0. This strictly positive value of y_{stop} suggests that the hottest point of the rod is ∼ 0.05 mm above the centre of the rod. We speculate that the cooling asymmetry can produce such a shift in the hottest point of the rod. In this case, a refined alignment of the diaphragm might imply an upward translation of t ≈ 50 μm above our current choice of centring. Fortunately, as this translation remains small (with t ≈ 50 μm < 75 μm = $\delta\rho_{stop}$), we can neglect this additional adjustment.

Moreover, for diaphragm alignment to be successful, all intra-cavity elements must be present inside the cavity. For example, our Acousto-Optic Modulator (AOM) deflects the beam downwards (by ∼ 1.5amin). In the absence of this AOM, a perfectly horizontal beam at the cavity exit would be obtained (in principle) with a horizontal cavity beam. As soon as this wedged AOM is present, the same horizontal exit beam requires a tilted cavity beam with a slope of ∼ tan(1.5amin). In this case, an upward displacement of the diaphragm of 87 μm would be required for the beam to still reach the centre of A0 (as {]DE] + (0.5 × A0_thickness) / n_{YAG} } × tan(1.5amin) ≈ 87 μm). This specific AOM wedge is a further reason for placing this diaphragm slightly above $y_{A0} = 0$ (to attenuate the downward slope of the laser out the cavity). However, as the nearby folding mirrors can compensate for this downward slope, we prefer to keep $y_{stop} \approx y_{A0} = 0$, to align the laser as closely as possible with the axis of each rod.

Fourthly, laserists generally align laser cavities by selecting the orientation of each element that minimises the Lasing Threshold (LT), in order to increase flashlamp life and obtain the best possible beam quality factor. This strategy is inadequate in terms of diaphragm centring (obtained here at maximum LT values). This specific situation leads to two recommendations: place the diaphragm as close as possible to the rod (to minimise decentring of the beam in relation to the rod during alignments), and realign the diaphragm according to the procedure in Table 5 if an annoying thermal drift occurs.

1.6. The choice of lenses and their tuning for two-colour lunar laser Ranging

This section justifies why our replacement of the E3 expander of (Martinot-Lagarde, 2016) by a much longer beam expander E2′= {Q + S} has considerably improved the collimation of the infrared beam.

Table 5
Lasing Threshold voltages (LT) with stop decentring relatively to A0 axis (8/03/2023).

y_{stop} (mm)	−1.15	−0.85	−0.55	−0.25	0.05	0.35	0.65	0.95
LT (V)	1515	1525	1540	1560	1592	1585	1590	1595
Cooling bias (V)	0	12	24	36	48	60	72	84
LT – bias (V)	1515	1513	1516	1524	1544	1525	1518	1511

Indeed, in the formalism of geometrical optics, a beam expander comprising two thin lenses of focal lengths $\{f_1 < 0;\ f_2 > |f_1|\}$ is afocal when its longitudinal length is $z = z_\infty = f_2 + f_1$. If $\Delta z = z - z_\infty$ with $|z - z_\infty| \ll f_2$, its effective focal length becomes:

$$f = \frac{(f_2 + \Delta z)\, f_2}{\Delta z} - \frac{(f_1 + f_2 + \Delta z)\, f}{|f_1|} \approx \frac{f_2^2}{\Delta z} - \frac{(f_1 + f_2)\, f}{|f_1|} \quad \Rightarrow \quad f \approx |f_1| \times f_2 / \Delta z \tag{12}$$

Numerically, as the infrared focal lengths are 1.025 times greater than the green ones, Eq. (12) procures infrared effective focal lengths of both expanders (f_{E3} and $f_{E2'}$) from their green afocal setting:

$f_{E3} \approx 1.025^2\, f_1\, f_2 / 0.025(f_2 + f_1) \sim -16.5$ m and that $f_{E2'} \approx 1.025^2\, f_1' \times f_2' / 0.025(f_2' + f_1') \approx -124$ m (where $f_1 = -220$ mm, $f_2 = 500$ mm, $f_1' = -1368.5$ mm and $f_2' = 2500$ mm). These focal lengths and the coudé length ($\Delta z_{coudé} \approx 12.3$ m) procure two estimators of the relative widening of the infrared beam along the coudé:

$$\frac{\Delta w}{\Delta z_{coudé}} \approx \frac{w}{f} \Rightarrow \frac{\Delta w}{w}(E3) \approx \frac{\Delta z_{coudé}}{f_{E3}} = \frac{12.3}{16.5} \approx 75\% \gg \frac{\Delta w}{w}(E2') \approx \frac{\Delta z_{coudé}}{f_{E2'}} = \frac{12.3}{124} \approx 9.9\% \tag{13}$$

Those two percentages are only indicative because of their geometrical optics formulation. However, it allows us to estimate that replacing E3 with E2′ improves the collimation of the infrared beam by an indicative factor of $75/9.9 \approx 7.6 \gg 1$, when the green beam is collimated in the coudé path. This huge factor justifies the fact that our current configuration is now capable of performing telemetry simultaneously at both wavelengths without vignetting. It also explains why (Courde, 2017) was forced to perform infrared LLR with vignetted pulses, which resulted in an experimental *IR/green transmission ratio of* 0.6 (as (Courde, 2017) performed LLR sessions with the E3 expander).

1.7. Two-colour lunar laser ranging results of 2023

This section presents 91 successful two-colour observations in 2023 and compares it to the 153 best infrared observations recorded during the same year as a function of the angular height of the Moon (h). In Fig. 4, we name those successful observations Normal Points (NPs). In the infrared, each NP is the average of N_1 echoes where $N_1 \geq 100$ (from 10 min × 10 Hz = 6000 laser shots), gathered from any of the five lunar *retro*-reflector. For the two-colour NPs, the plot contains all our successful observations (where 21 of them comprised simultaneously $N_2 \geq 60$ green echoes and $N_1 \geq 60$ infrared echoes).

Here, the two-colour NPs curve grows with h, unlike the infrared curve (which is almost flat). This positive slope is mainly due to the atmospheric transmission of visible lasers with the angular height (h) of the space target, whereas the transmission of infrared light remains almost insensitive to h (Degnan, 1993).

More precisely, we remark that two-colour LLR successes increase specifically when the angular height of the Moon rises from 32° to 66°. It raises a double question: why is it so difficult to succeed in two-colour LLR below h = 32°; and why is this success so stable above 66°?

We propose to deal with this question by introducing two positive angles α(h) and θ. α(h) is the differential atmospheric refraction angle, which is also the angle of separation between the centres of the green and infrared laser footprints on the Moon (as shown on the right of Fig. 4). θ is the minimum value between the far field divergence of the infrared beam (θ_1) and of the green beam (θ_2). We get:

- if α(h)/θ < 1, beam footprints centres are close ⇒ we expect stable success for two-colour LLR,
- if α(h) ~ θ, the two-colour LLR success rate is very sensitive to those intermediate values of α,
- if α(h) / θ > 1, two-colour LLR success disappears due to excessive footprints separation.

The precise determination of θ is beyond the scope of this study, as it requires measuring the exact wavefront of our real laser in the far field, as proposed by (Burris, et al., 2013). However, we can evaluate it with the Paraxial Gaussian Beam Divergence (GBPD) operand of *Zemax* applied to the configuration in Table 2,

$$\text{where: } \theta_1 = 1.709\text{as and } \theta_2 = 0.601\text{as} \Rightarrow \theta = \min(\theta_1; \theta_2) = \theta_2 \approx 0.6\text{as} \tag{14}$$

We are aware that those *Zemax* calculations underestimate the real value of θ, which means that all footprints in Fig. 4(a, b) hold for calm sky conditions, with low Seeing values ($S < S_{mean} \approx 1.09$as (Aristidi, 2019).

As regards the differential atmospheric refraction, $\alpha = \alpha_2 - \alpha_1 > 0$ because the atmospheric refraction deflects more the green light (with α_2) than the infrared light (with α_1). α increases with the zenith angle of the target ζ, where those four angles $\{\alpha, \alpha_2, \alpha_1, \zeta\}$ have the same downward orientation.

In practice, α_2 vanishes experimentally if the operator centres a

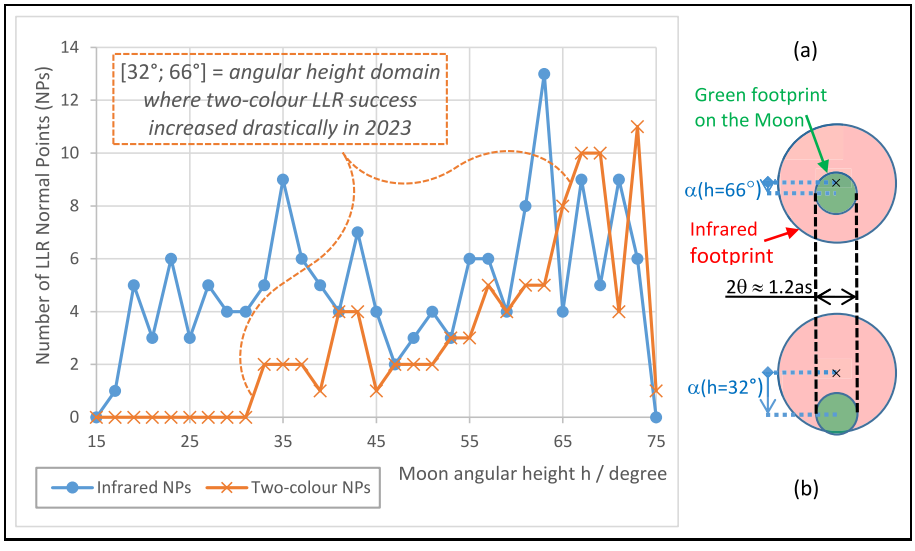

Fig. 4. LLR **N**ormal **P**oints recorded in 2023 and beam footprints on the Moon at h = 66°(a) or 32°(b).

Table 6
Δα estimator of the differential refraction as a function of the angular height of the Moon (h).

h	15°	24°	**32°**	40°	50°	58°	**66°**	75°
ζ = 90° − h	75°	66°	58°	50°	40°	32°	24°	15°
Δα = 3.68μrad × tanζ	2.83as	1.71as	**1.22as**	0.91as	0.64as	0.47as	**0.34as**	0.2as

visible lunar crater or a nearby star on the telescope axis before green ranging. He benefits here from the proximity of λ_2 to the centre of the visible spectrum (~580 nm). Then, best infrared LLR needs a downward tip of the telescope of α.

The differential atmospheric refraction is based on knowledge of the refractive indices of the air at each wavelength. As B. Edlén (Edlén, 1966) measured it in laboratory (up to the 8th digit at 15 °C, 1013.25 hPa and in dry air), we propose to use the same atmospheric conditions with the exception of the pressure of ~ 880 hPa, to take account of the reduced atmospheric pressure at the station altitude of ~1300 m.

The **I**nternational **A**stronomical **U**nion **S**tandards **O**f **F**undamental **A**stronomy Board (IAU SOFA Center) publishes software for estimating the atmospheric refraction (Subroutine iau_REFCO, 2021). We used the 2021-May-12 release of this software, which calculates chromatic atmospheric refraction from ground pressure, temperature and humidity. As our analysis focuses on the most favourable LLR observations (where the weather is generally the driest), we choose to neglect humidity. Moreover, as humidity slightly reduces refraction (Dettwiller, 2204), this choice of dry air, which slightly overestimates this refraction effect, is the extreme experimental situation that we have to take into account (as regards this refraction impact).

In dry air, the respective refractive indices of the air (in Calern) at λ_1 and λ_2 are $n_1 = 1.00023794$ and $n_2 = 1.00024162$. With $n_3 = 0.5\ (n_1 + n_2) = 1.00023978$, the SOFA refraction angle is (in radians):

$$\alpha_{SOFA}(n_3) = (n_3 - 1)\left\{(1-\beta)\tan\zeta - \left[\beta - \frac{n_3 - 1}{2}\right](\tan\zeta)^3\right\} \quad (15)$$

with $\beta = 4.4474 \times 10^{-6} \times (273.15 + T) = 4.4474 \times 10^{-6} \times (273.15 + 15\ °C) \approx 1.28 \times 10^{-3}$ (16)

$$\Rightarrow \alpha_2 - \alpha_1 \approx (n_2 - n_1)\frac{d\alpha_{SOFA}(n_3)}{dn_3} \approx (n_2 - n_1)\tan\zeta\left\{1 - \beta - [\beta - (n_3 - 1)](\tan\zeta)^2\right\} \quad (17)$$

where $0 < \beta + [\beta - (n_3 - 1)] \times (\tan\zeta)^2 \leq \beta + [\beta - (n_3 - 1)] \times [\tan(75°)]^2 \approx 0.016 < 2\ \%$ if $\zeta \leq 75°$ (18)

Eq. (17–18) $\Rightarrow 0.98\ (n_2 - n_1)\tan\zeta < \alpha = \alpha_2 - \alpha_1 < (n_2 - n_1)\tan\zeta = \Delta\alpha$ (19)

So, Δα estimates appropriately the differential refraction angle α(h) for Moon angular heights ≥ 15°.

Combining Table 6 results with θ ≈ 0.6as illustrates well the α/θ ratio impact on two-colour LLR:

- When h ≥ 66°, α/θ ≤ Δα(h = 66°)/θ ≈ 0.57 < 1. This near-centring of the green footprint inside the infrared one favours two-colour LLR, justifying a stable success for two-colour LLR in 2023.
- When 32° < h < 66°, α/θ ∈]0.57; 2.03[, two-colour LLR success increases with h in 2023. This situation coincides precisely with the zone where α specifically influences the two-colour LLR success rate (because the green footprint gradually escapes from the axis of the infrared laser).
- When h ≤ 32°, α/θ ≥ 2.03 > 1, this *Zemax* modelling procures an excessive footprint separation, which is consistent with our systematic failure in two-colour LLR for h ≤ 32° in 2023.

Finally, we desire to point out that the chromaticity of lens V separates its longitudinal position minimising the green beam divergence from the tuning minimising the infrared divergence of ~ 16 mm. The best two-colour setting (exposed in Table 2) is not in the middle of this interval but it is 3 times nearer to the green collimation case than to the infrared collimation case. This illustrates that infrared LLR is much easier, as photonic, atmospheric, corner-cubes and sunlight effects (Chabé, 2020; Courde, 2017) allow triple-sized infrared lunar imprints, greatly facilitating the illumination of any selected lunar retroreflector:

– indeed, when the sky is especially calm, Eq. (14) defines a green laser footprint on the Moon of minimal radius of: $s(z_{Moon}) \approx Earth\_Moon \times \tan(\theta_2) \approx 380000\ km \times \tan(0.601as) \approx 1.11\ km$ (20)

– and the infrared beam of this laser converges first in the atmosphere but diverges mainly in space, leading to: $w(z_{Moon}) \approx Earth\_Moon \times \tan(\theta_1) \approx 380000\ km \times \tan(1.709as) \approx 3.15\ km$ (21)

2. Conclusion

This article describes the evolution of the laser configuration at the MéO station since 2016. It exposes how we improved the pointing stability of the laser source (and its co-alignment with the telescope), while preserving the size and fluence of the green beam, so that the downstream optical configuration of the MéO station has remained unchanged (as regards its operational SLR and LLR activities). Concerning the infrared beam shape, the main change occurred inside the coudé path, where its collimation improved considerably, in contrast to 2016, when a local infrared divergence deprived the laser of 40 % of its infrared energy emitted towards the space target (Courde, 2017). Despite this, (Chabé, 2020; Courde, 2017) managed to establish that the implementation of an infrared channel effectively increased the sensitivity and the accuracy of our LLR observations from 2015. For example, (Courde, 2017) compared LLR observations (made during 2014–2016), that showed a correct concordance with theoretical estimations of each link budget, with stating the same ~ 20 % quantum efficiency in both wavelengths (using Single-Photon Avalanche Diodes). This was very promising regarding the benefits of infrared LLR. However, these analyses left out the challenge of tuning MéO to achieve two-colour LLR, which we specifically addressed here.

The present study characterizes the evolution of the beam from the laser cavity to the Moon, using the circularised Gaussian beam formalism of the *Zemax* software. It extends the analysis of (Martinot-Lagarde, 2016), which focused mainly on the amplification chain. This refined analysis demonstrated that the quality factor of the beam (presumed achromatic) increases from $M^2 \sim 1.03$ inside the cavity to $M^2 \sim 1.17$ in space, in favourable observing conditions (where all sources of laser broadening remain negligible).

This LLR analysis selected 153 infrared Normal Points (NPs) and 91 two-colour NPs. These 244 successful LLR sessions (lasting 10 min and done at a 10 Hz rate) required 244 × 6000 = 1464 thousand laser shots. It represents 1464 / 20,000 ≈ 7.3 % of the annual MéO {SLR + LLR} results usually delivered to ILRS. This big amount of exceptional observations enabled us to determine that the best configuration (maximising two-colour LLR) was with a full-angle divergence of the green beam of ~ $2\theta_2 \approx 1.2as$.

Finally, we estimate that an eventual increase of the actual chromatism of lens V would not enable to extend MéO sky coverage for two-colour LLR below 32°, as extending the actual full-angle divergence of

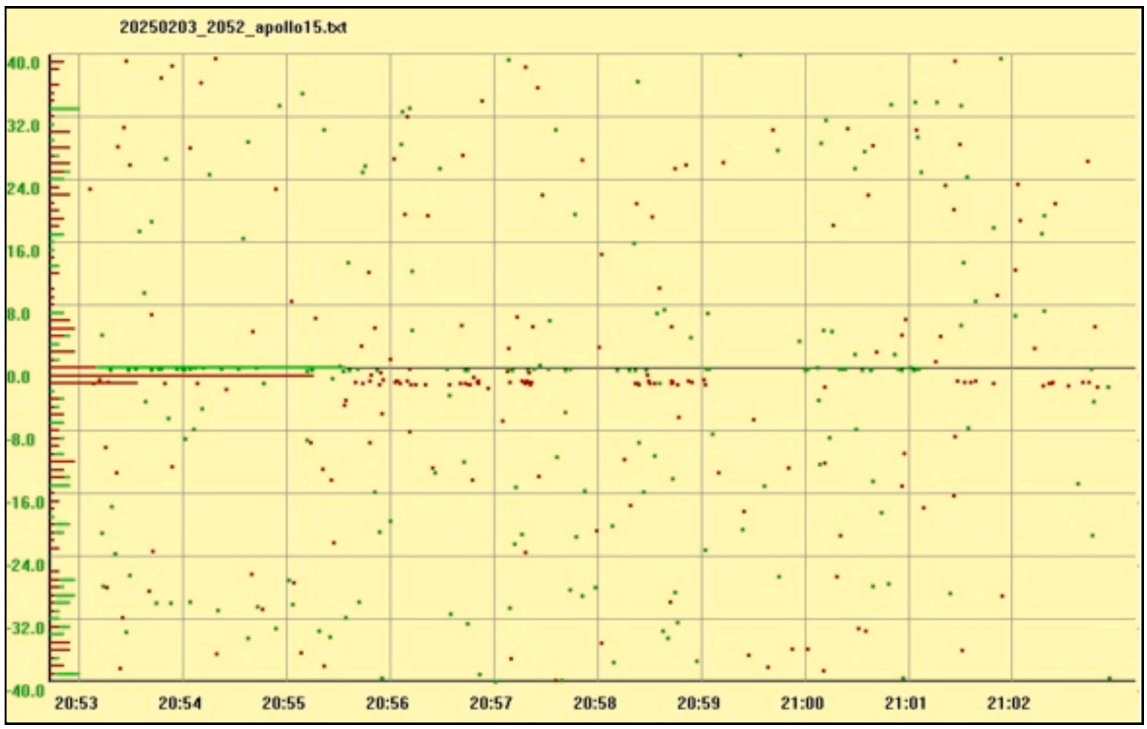

Fig. 5. Two-colour LLR session on Apollo15, realised on the 03 February 2025 with h ~ 19°.
The horizontal axis is the UTC observing time. The vertical axis dates LLR echoes in ns.
Green echoes are green {dots + histogram}. Infrared (IR) echoes are red {dots + histogram}:
→ *Green residual* = {green_2_way_time_of_flight – green pulse travel prediction} = − 0.1 ns,
→ *Infrared residual* = {IR_2_way_time_of_flight – green pulse travel prediction} = − 1.9 ns.
Here, the *Earth-Moon ranging accuracies (one-way RMS)* are 12.8 mm@532 nm & 29.4 mm@1064 nm.

the infrared beam above its actual value of $2\theta_1 \approx 3.4$as would dilute too much its lunar fluence. Therefore, we recommend two perspectives to extend our two-colour LLR sky coverage. One could insert Risley prisms in the emission path of the laser to cancel out the differential refraction effect (to superimpose both lunar footprints). Alternatively, a higher rate laser could allow operators to alternate several short (~1min) green and infrared LLR observations, with the centre of each beam alternatively aimed at the selected lunar retroreflector. The average of those observations in each wavelength would give access to two Normal Points (for a conventional session duration of ~ 10 min).

We recently tested this second alternative (with our 10 Hz laser) during a very favourable night (3 February 2025 at 20H52TU), with a Moon elevation h ~ 19°. During this specific observation (shown on Fig. 5), we centred the green beam on Apollo 15 during 3 sub-periods = { [~20H53; ~20H55] ∪ [~20H57; ~20H58] ∪ [~20H59; ~21H01] }. We also optimised the infrared echoes reception during the remaining time of this 10 min session (with taking into account the differential refraction effect).

As awaited, the gathering of those echoes was highly sequential because of the high strength of the differential refraction (as $\alpha(h = 19°) / \theta \approx 3.67 > 1$). This experimental alternation of green and infrared echoes clearly attests that the differential refraction separates both imprints on the Moon below 32°.

Moreover, this specific screenshot is very instructive to compare the link budget in each wavelength. Let us recall that we performed this experiment with a two-colour laser, emitting pulses of 200 mJ in the green and of 100 mJ in the infrared. As green photons are twice more energetic than infrared ones, this gives the same number of photons emitted by the telemeter in each wavelength. As we also centred each beam on Apollo 15 during a similar duration (of ~ 5 min), the ratio of echoes collected in each colour = $N_1/N_2 = 65/56 \approx 1.16$ illustrates our typical advantageous LLR link budget in the infrared. This is the reason why MéO operators are advised to initiate their LLR activity in the infrared, even though infrared echoes comprise a higher timing jitter (generating the wider red histogram in Fig. 5).

CRediT authorship contribution statement

G. Martinot-Lagarde: Writing – review & editing, Writing – original draft, Validation, Software, Methodology, Investigation, Formal analysis, Data curation, Conceptualization. **H. Mariey:** Validation. **N. Maurice:** Writing – original draft. **J. Scariot:** Validation. **H. Viot:** Validation.

Declaration of competing interest

The authors declare that they have no known competing financial interests or personal relationships that could have appeared to influence the work reported in this paper.

Acknowledgments

We thank the CNRS-INSU for its annual funding.

Data availability

Data will be made available on request.

References

Aristidi, E., et al., 2019. A generalised differential image motion monitor. MNRAS 486, 915–925.
Burris R. et al. *18th ILRS Workshop, Tokyo, Japan* 2013 ; **8** : 13-03-06-Burris.pdf.
Chabé, J., et al., 2020. Recent progress in lunar laser ranging at Grasse laser ranging station. Earth Space Sci. 7 e2019EA000785.
Courde, C., et al., 2017. Lunar laser ranging in infrared at the Grasse laser station. A&A 602, A90.

Degnan, J.J., 1993. Contributions of Space Geodesy to Geodynamics: Technology "Millimeter Accuracy Satellite Laser Ranging: a Review. Geodynamics 25, 140.
Dettwiller L. Short review on the refractive index of air as a function of temperature, pressure, humidity and ionization. arXiv:2204.02603 [physics.optics] https://doi.org/10.48550/arXiv.2204.02603.
Edlén, B., 1966. The refractive index of air. Metrologia 2, 71.
Koechner, W., 1970. Thermal lensing in a Nd:YAG laser rod. Appl. Opt. 9 (11), 2548–2553.
Lucchini C. Télémétrie laser deux couleurs. Thèse UNS, 1995, N°95 NICE 4914.
Martinot-Lagarde, G., et al., 2016. Laser enhancements for lunar laser ranging at 532nm. Resul. Phys. 6, 329–336.
Murphy, T.W., 2013. Lunar laser ranging: the millimetre challenge. Rep. Prog. Phys. 76, 076901 (21).
Samain E. et al. *Astronomy & Astrophysics Supplement Series* **130** (1998) 235-244.
Subroutine iau_REFCO, https://www.iausofa.org/2021_0512_F/sofa/refco.for , from the "Software Routines from the IAU SOFA Collection, (http://www.iausofa.org)".
Yee, T.K., et al., 1979. Simmer-enhanced flashlamp-pumped dye laser. Appl. Opt. 18 (8), 1131–1132.